

# Computational study of early-time droplet impact dynamics on textured and lubricant-infused surfaces

Nathaniel I.J. Henman<sup>a,b</sup>, Frank T. Smith<sup>b</sup>, Manish K. Tiwari<sup>a,c,\*</sup>

<sup>a</sup> Nanoengineered Systems Lab, Department of Mechanical Engineering, University College London, London, UK

<sup>b</sup> Department of Mathematics, University College London, London, UK

<sup>c</sup> Wellcome/EPSCRC Center for Interventional and Surgical Sciences, University College London, London, UK

## ARTICLE INFO

### Keywords:

Droplet impact  
Lubricant-infused surfaces  
Interfacial flows  
Numerical simulation

## ABSTRACT

The high-speed impact of liquid droplets onto surfaces with different properties is a vast area of research. The present study focuses on using numerical simulation to investigate the delicate early stages of droplet impact onto both textured and lubricant-infused surfaces. An idealised two-dimensional model is utilised for a normal impact of an incompressible liquid droplet onto a surface of rectangular asperities and a thin layer of lubricant. In experiments the length scale of the impinging droplet is typically much larger than that of the surface asperities. The study here aims to complement such work by considering the same scaling, with millimetre sized droplets impinging on surfaces with micrometre sized asperities. It is found that variations of the surface properties have an insignificant effect on the location of the jet root and all dynamical changes are focused in the thin splash jet ejected at impact. The effects that the parameters pertaining to a lubricant-infused surface, namely the surface topology, lubricant depth and lubricant viscosity, have on the extent of the thin splash jet are investigated in turn. Increasing the gap between the surface asperities results in a reduction in the horizontal extent of the splash jet, while variations in lubricant depth and viscosity exhibit non-monotonic effects. In each case phase diagrams are presented to characterise the early time splashing behaviour and investigate the influence of impact velocity. Comparisons of a lubricant-infused surface to a superhydrophobic surface, with no lubricant present, highlight the importance of the surface topology. The results presented in this manuscript also highlight possible avenues of further research, both analytical and experimental, as well as aid in the design of novel non-wetting surfaces.

## 1. Introduction

Engineered surfaces that are able to control the dynamics of droplet impacts are an increasingly important area of research in today's world. Droplet impacts occur in a tremendous amount of industrial situations such as anti-icing (Kim et al., 2012; Wang et al., 2016), spray coating (Fauchais et al., 2004) and fuel combustion (Moreira et al., 2010), to name but a few. Being able to control the droplet impact using surface engineering (Maitra et al., 2014a,b) can be hugely desirable. Over the last decade, with inspiration from nature (Zeng et al., 2021), there has been a large increase in attention to so-called lubricant-infused surfaces, where low surface tension lubricants are infused into porous or textured surfaces (Li et al., 2019; Preston et al., 2017; Sett et al., 2017). These surfaces have been found to have excellent anti-icing (Kim et al., 2012) and anti-biofouling (Zhang et al., 2017) properties. In this paper, we use numerical simulation to study the normal impact of a millimetre sized droplet onto a lubricant-infused surface with micrometre sized asperities. The aim of the present study

is to build upon earlier experimental (Kim and Rothstein, 2016; Muschi et al., 2018) and numerical (Yeganehdoust et al., 2021) work on droplet impact on lubricant-infused surfaces, with novelty arising from the consideration of splashing behaviour and the surface parameters considered, namely the surface morphology, the lubricant depth and the lubricant viscosity.

Lubricant-infused surfaces became of interest from seeking alternatives to superhydrophobic surfaces, as well as through the inspiration of surfaces seen in nature. Superhydrophobic surfaces, despite all their beneficial attributes (Antonini et al., 2011), do have weaknesses such as repellency only of liquids of relatively high surface tension, weak pressure stability and low mechanical stability. Methods to alleviate these drawbacks of superhydrophobic surfaces were explored by Quéré (2005) and further investigated by Wong et al. (2011) and Smith et al. (2013), showing lubricant-infused surfaces to have excellent anti-wetting properties and pressure stability. Lubricant-infused surfaces

\* Corresponding author at: Nanoengineered Systems Lab, Department of Mechanical Engineering, University College London, London, UK.  
E-mail addresses: [f.smith@ucl.ac.uk](mailto:f.smith@ucl.ac.uk) (F.T. Smith), [m.tiwari@ucl.ac.uk](mailto:m.tiwari@ucl.ac.uk) (M.K. Tiwari).

mimic surfaces seen in nature, such as the *Nepenthes* pitcher plant surface (Bohn and Federle, 2004). This slippery surface has evolved to be able to capture insects easier as they slide into the plant's interior.

Droplet impact studies with lubricant-infused surfaces have received little attention currently, both experimentally and numerically. Muschi et al. (2018) examined the effect of varying the depth of the lubricant layer of the surface on droplet impact dynamics. A spin coating method was used to control the thickness of the lubricant and it was found that the wettability and spreading and retraction dynamics were not greatly affected by the change in lubricant thickness, so long as the surface remained mostly homogeneous. The effect of the lubricant viscosity was investigated by Kim and Rothstein (2016), where it was found that lowering the lubricant viscosity led to an increase in the spreading and retraction velocities of a droplet impact, as well as the maximum spreading diameter. The lubricant viscosity was similarly tested by Lee et al. (2014), who found that the stability of the lubricant inside the nanotextured surface was improved by increasing the lubricant viscosity. While the above studies concentrated on passive methods for controlling the droplet impact dynamics, a recent study by Biroun et al. (2021) focused on using surface acoustic waves as a way of actively controlling the droplet impact dynamics. They found that by applying surface acoustic waves to the droplet the contact time was reduced. Using a numerical approach, Yeganehdoust et al. (2021) considered the impact of a micro-droplet onto different micro-textured surfaces. They compared results between a superhydrophobic surface and a lubricant-infused surfaces, where the textures are filled with lubricant, and found that droplet repellency and mobility on lubricant-infused surfaces were improved on low-density micro-textures surfaces compared to superhydrophobic surfaces.

In the present study, we aim to numerically examine the delicate early stages of droplet impact, with emphasis on the splash jet that is emitted at the point of impact. This splash jet is observed experimentally (Howland et al., 2016; Riboux and Gordillo, 2014) and also predicted by the well established asymptotic structure known as Wagner theory (Scolan and Korobkin, 2001; Wagner, 1932). Wagner theory has been shown to accurately predict the radius of the wetted region for droplet impacts (Riboux and Gordillo, 2014) (or, the location of the jet root) as well as exhibiting excellent agreement with numerical simulations (Cimpeanu and Moore, 2018). Extensions to Wagner theory include considerations of surface deformability (Khabakhpasheva and Korobkin, 2020; Negus et al., 2021; Pegg et al., 2018) and roughness elements (Ellis et al., 2011) as well as surface water (Howison et al., 2005) and ice formation (Elliott and Smith, 2017). Recently, Hicks (2022) performed a study on a wide variety of continuous non-flat surfaces, using Wagner theory to predict the leading order free-surface shapes near impact. His model is able to go close to replicating the influence of a textured surface on droplet impacts, with the caveat that the surface shape must be continuous, without vertical surface elements. The use of analytical methods such as Wagner theory has so far been unable to model the leading order solution or the thin splash jet for droplet impacts onto significantly textured, superhydrophobic surfaces (and, extending further, lubricant-infused surfaces). To that end, we will utilise direct numerical simulation to study the delicate early stages of droplet impact on lubricant-infused surfaces in order to access parameters unavailable to Wagner theory. So far a detailed study of the early stages of impact when the depth of the surface asperities are of the same order as the thickness of the splash jet has not been performed. Our results will complement previous experimental results, which are commonly performed as a millimetre sized droplet impinging on a surface with micrometre sized asperities (Kim and Rothstein, 2016; Muschi et al., 2018), a situation in which the comparable scales of the splash jet thickness and the surface asperities are likely to hold (Howison et al., 2005).

Two-dimensional studies of droplet impact and splashing on flat surfaces have been shown to be a reasonable approximation of the very much three-dimensional problem (Wu and Cao, 2017). Despite the clear

geometrical discrepancies, two-dimensional droplet impact dynamics on flat surfaces are qualitatively very similar to experimental studies, a matter which will be discussed below. The extension of this to textured surfaces remains an open question, due to the lack of axisymmetry exhibited by the surface. However, using a two-dimensional many-body dissipative particle dynamics method, Wang et al. (2017) were able to show close agreement on splashing with experimental results. As a first approximation, a two-dimensional study of the delicate early stages of droplet impact on textured and lubricant-infused surfaces is hugely important to the initial understanding of this problem and has not been reported previously in the literature. We make approximate, qualitative conclusions on the impact of our results in reality, and do believe our results build a basis for new research in the area.

The layout of this paper is as follows: in Section 2 the governing equations and relevant parameters will be introduced, then in Section 3 the computational methods for solving these and computational domain information are given. After that, in Section 4 the results will be presented. First, we will systematically study the influences of parameters pertaining to lubricant-infused surfaces alone. Then, a comparison will be made to effects on textured, superhydrophobic surfaces. Finally, Section 5 will contain the conclusions.

## 2. Model setup and governing equations

Suppose a two-dimensional Cartesian circular liquid droplet of radius  $R$  approaches normally a rectangular textured surface with a downward velocity  $V$ . The geometry of the textured surface is characterised by three lengths; the height  $H$ , the width  $W$  and the gap  $G$ . The textures are filled up to a depth  $\delta$  with a lubricant. Fig. 1 shows a schematic of the problem, with the physical parameters labelled.

We are considering here a three phase fluid flow problem. The three phases to consider are the liquid droplet, the surrounding air and the lubricant. Each phase will be considered as an incompressible Newtonian fluid with density  $\rho_i$  and dynamic viscosity  $\mu_i$  for  $i = l$  (liquid droplet),  $i = g$  (surrounding air) and  $i = LIS$  (lubricant), where  $LIS$  stands for "lubricant-infused surface". The surface tension between the liquid droplet and the air will be written  $\sigma_{l,g}$ , between the liquid droplet and the lubricant will be  $\sigma_{l,LIS}$  and between the air and the lubricant will be  $\sigma_{g,LIS}$ . The effects of gravity are assumed to be negligible and are not included in the simulations.

The fluid flow is modelled by the Navier–Stokes equations

$$\frac{\partial}{\partial t}(\rho \mathbf{u}) + \nabla \cdot (\rho \mathbf{u} \mathbf{u}) = -\nabla p + \nabla \cdot (\mu (\nabla \mathbf{u} + \nabla \mathbf{u}^T)) + \mathbf{F}, \quad (1a)$$

$$\frac{\partial \rho}{\partial t} + \nabla \cdot (\rho \mathbf{u}) = 0, \quad (1b)$$

where  $t$  is time,  $\nabla = (\partial/\partial x, \partial/\partial y)$  is the two-dimensional gradient operator,  $p$  is the pressure,  $\mathbf{u} = (u, v)$  is the velocity vector, where  $u$  is the horizontal and  $v$  the vertical components, and  $\mathbf{F}$  is the surface tension force. In order to accurately capture the free-surface of both the droplet and the lubricant, Eq. (1) are solved in conjunction with a volume-of-fluid (VOF) method. The VOF method defines a volume fraction of each of the three phases at each point in the domain and calculates the properties of the fluid at each point based on this volume fraction, as follows. The sum of the volume fractions of all three phases is equal to one everywhere,

$$\alpha_l + \alpha_g + \alpha_{LIS} = 1. \quad (2)$$

Now, the density  $\rho$  and viscosity  $\mu$  in the Navier–Stokes equations (1) are defined everywhere by

$$\rho = \alpha_l \rho_l + \alpha_g \rho_g + \alpha_{LIS} \rho_{LIS}, \quad (3a)$$

$$\mu = \alpha_l \mu_l + \alpha_g \mu_g + \alpha_{LIS} \mu_{LIS}. \quad (3b)$$

The values of density  $\rho$  and viscosity  $\mu$  vary across regions in which the fluid interfaces pass through. Hence, gradients of each need to be considered and so the Navier–Stokes equations (1) are solved to

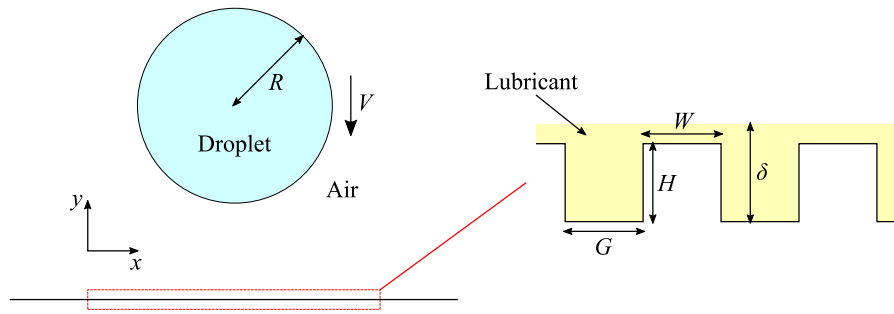


Fig. 1. Schematic of the physical model set up with a textured surface.

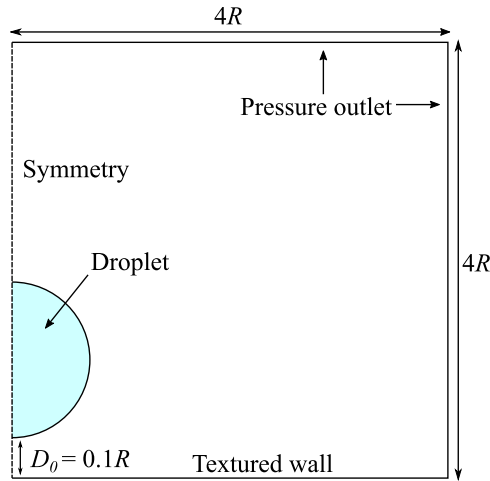


Fig. 2. Schematic showing the numerical domain and the boundary conditions.

account for non-constant  $\rho$  and  $\mu$ . The evolution of the free surfaces of the droplet and the lubricant are calculated using the volume fraction equation

$$\frac{\partial \alpha_i}{\partial t} + \nabla \cdot (\alpha_i \mathbf{u}) = 0 \quad (4)$$

for  $i = l, LIS$ . Finally here, the surface tension force  $\mathbf{F}$  is calculated using the continuum surface force model (Brackbill et al., 1992), which, for a three phase system, is formulated as

$$\mathbf{F} = \sum_{\text{pairs } i,j, i \neq j} \sigma_{i,j} \frac{\alpha_i \rho_i \kappa_j \nabla \alpha_j + \alpha_j \rho_j \kappa_i \nabla \alpha_i}{\frac{1}{2}(\rho_i + \rho_j)}, \quad (5)$$

where the pairs  $ij$  are given by the three distinct pairs of the different interfaces and  $\kappa_i$  is the curvature of the interface, given by

$$\kappa_i = -\nabla \cdot \left( \frac{\nabla \alpha_i}{|\nabla \alpha_i|} \right). \quad (6)$$

### 3. Computational setup

The present study considers a water droplet ( $\rho_l = 10^3 \text{ kg m}^{-3}$ ,  $\mu_l = 10^{-3} \text{ Pa s}$ ) in air ( $\rho_g = 1.2 \text{ kg m}^{-3}$ ,  $\mu_g = 1.8 \times 10^{-5} \text{ Pa s}$ ) of radius  $R = 1 \text{ mm}$ . It is assumed that the lubricant is a member of the Krytox series of lubricants, with a density of  $\rho_{LIS} = 1.85 \times 10^3 \text{ kg m}^{-3}$  and a vast range of viscosities (Peppou-Chapman et al., 2020). The surface tension coefficients between the interfaces are taken as  $\sigma_{l,g} = 7.3 \times 10^{-2} \text{ N m}^{-1}$ ,  $\sigma_{l,LIS} = 5.3 \times 10^{-2} \text{ N m}^{-1}$  and  $\sigma_{g,LIS} = 1.7 \times 10^{-2} \text{ N m}^{-1}$ . For the Krytox series of lubricant, despite vast varieties of viscosities, the surface tension between the lubricant and the air/water remains roughly constant (Peppou-Chapman et al., 2020).

We exploit the symmetry of the problem and only calculate the right half of the droplet. The numerical domain on which our calculations are

performed is a two-dimensional square box with sides of length  $4R = 4 \text{ mm}$ . The surface texturing is achieved by having small rectangular domains appended onto the bottom of the domain at  $y = 0$ , protruding into  $y < 0$ , resulting in  $y = 0$  being the top of the textures. The boundary conditions on the top and right side of the domain are set as pressure outlets, the left side of the domain is a symmetry boundary and the bottom, including all the sides of the appended rectangles, is set to an impenetrable wall condition, with no slip. To ensure consistency within our results and to keep the symmetry,  $x = 0$  is always located in the middle of a pillar. A schematic showing the computational domain and boundary conditions is shown in Fig. 2.

In order to more closely mimic previous experimental studies (Kim and Rothstein, 2016; Muschi et al., 2018), we wish to consider cases where  $W, H, G \ll R$ . For brevity, we only vary the distance between the pillars  $G$ , and henceforth fix  $W = H = 10 \text{ }\mu\text{m}$ .

The three phase fluid flow problem, governed by Eqs. (1)–(6), is solved in the described computational domain using the CFD code ANSYS Fluent v19.5. The pressure–velocity coupling is performed using the PISO algorithm and spatial discretisation of the Navier–Stokes equations is done using the QUICK scheme. For pressure discretisation the PRESTO scheme is used. The spatial discretisation of the volume fraction equation is done using the geometrical reconstruction scheme. A first order implicit method is used for the unsteady terms in the Navier–Stokes equations, with a variable time step. The variable time step is based on the Courant number, which is kept below 0.2 for all simulations. The code advances to the next time step when the scaled residuals of the continuity and momentum equations are below  $10^{-4}$ . The effect of dynamic wetting is not considered in the study, thus a static contact angle between each of the three phases is set as  $\pi/2$ . During the spreading phase of droplet impact, when inertial effects are dominant, various authors have reported that dynamic wetting is unimportant (Delele et al., 2016; Pasandideh-Fard et al., 1996; Philippi et al., 2016). In cells where all three phases are present, the angles between the interfaces of each phase are determined through the continuum surface force model (Brackbill et al., 1992).

The square domain box is divided into three regions: a triangular mesh region, a square mesh region and a refined mesh region which encapsulates the subsequent splash jet after impact, where the square mesh cells are decreased in size by a factor of two. Fig. 3 gives an example of the mesh used in the simulations, including the initial droplet shape and position, as well as an enlarged image of the mesh in the refined region near the impact sight. A mesh independence study was carried out on five different mesh sizes, as well as a case where the domain sides are doubled to  $8R$  (calculated on the standard mesh size), as summarised in Table 1, for a test case with pillar spacing  $G/R = 0.01$ , initial lubricant depth  $\delta/H = 1$  and lubricant viscosity ratio  $\mu_{LIS}/\mu_l = 30$  at  $We = \rho_l V^2 R / \sigma_{l,g} = 70$ . The non-dimensional variation in the horizontal extent of the splash jet, a key metric in our study (see Fig. 7(b) for definition), in time for the six different meshes is shown in Fig. 4. Excellent agreement is found between the standard mesh and further refinements, as well as with the  $8R \times 8R$  domain. From here on-wards, the standard mesh (domain size  $4R \times 4R$ ) is used

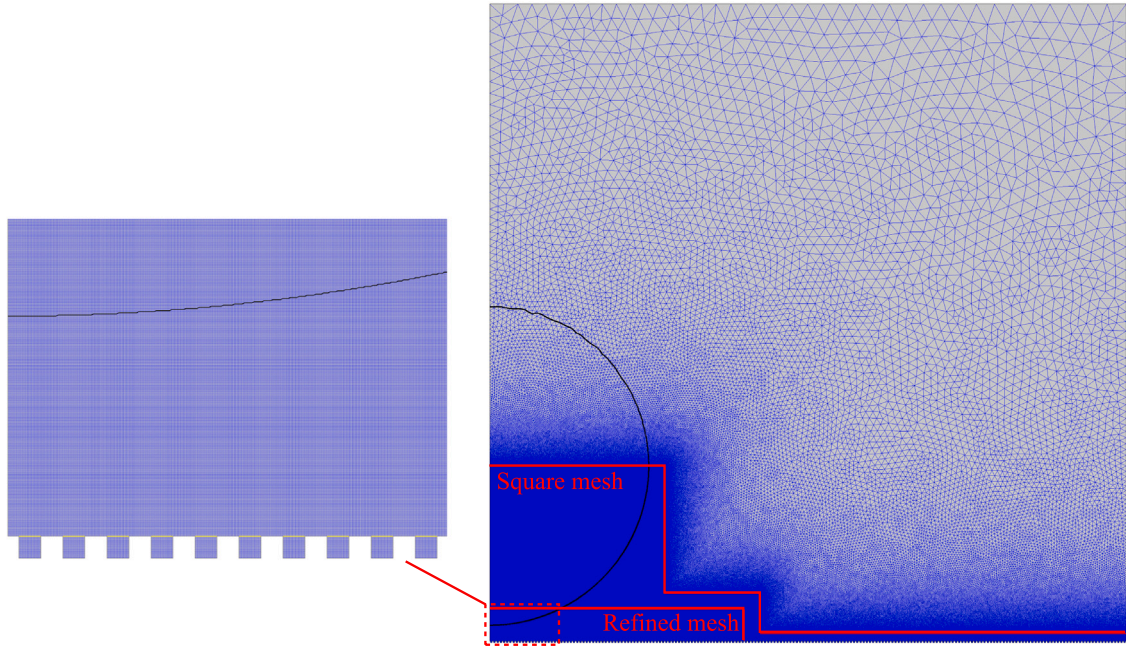


Fig. 3. An example of the mesh used in the simulations, including initial droplet shape and position.

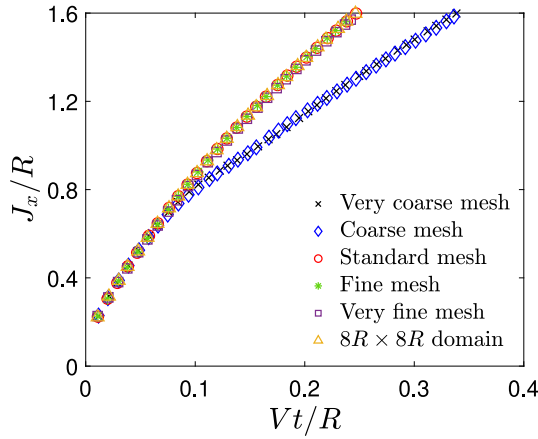


Fig. 4. The non-dimensional variation in time of the horizontal extent of the splash jet  $J_x/R$  for pillar spacing  $G/R = 0.01$ , lubricant depth of  $\delta/H = 1$  and lubricant viscosity  $\mu_{LIS}/\mu_l = 30$  at  $We = 70$ , calculated on the five different meshes listed in Table 1.

in all simulations. Detailed data for the initial extent of the splash jet for droplet impact on textured or lubricant-infused surfaces is currently not available in the literature. Nevertheless, we will make connections to available experimental results in the text that follows. Experimental data for the jet evolution in the early stages of impact is available for flat surfaces (Riboux and Gordillo, 2014). Fig. 5 gives a qualitative comparison between our two-dimensional results and experimental results (Riboux and Gordillo, 2014), for a water droplet impact on a flat surface at  $We = 98$  and  $Re = \rho_l V R / \mu_l = 3462$ . Despite clear discrepancies due to geometrical differences, with our simulation overpredicting the extent of the splash jet, the two results are qualitatively similar and the jet extent in both cases appears to evolve proportionally to  $(Vt/R)^{3/5}$ . This qualitative similarity between the two-dimensional simulation and the experimental data is highlighted by plotting this data on a log-log scale in the inset of Fig. 5. As further validation, we also plot the results for the extent of the splash jet when calculated on a three-dimensional axisymmetric grid, which has excellent agreement with the experimental results. We are therefore confident in the

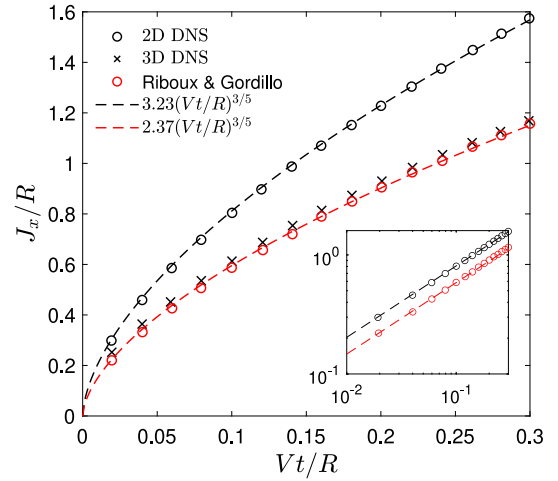


Fig. 5. Comparison of two-dimensional and three-dimensional simulation results for the jet horizontal extent  $J_x/R$  to experimental results from Riboux and Gordillo (2014) for a water droplet impact on a flat surface at  $We = 98$  and  $Re = 3462$ . The inset shows the two-dimensional simulation and the experimental data but on a log-log scale.

Table 1

Details of the five different meshes used in the mesh independence study.

Mesh	Refined mesh size	Total cells
Very coarse	0.625 $\mu\text{m}$	$1.77 \times 10^6$
Coarse	0.556 $\mu\text{m}$	$2.34 \times 10^6$
Standard	0.5 $\mu\text{m}$	$2.72 \times 10^6$
Fine	0.417 $\mu\text{m}$	$4.03 \times 10^6$
Very fine	0.357 $\mu\text{m}$	$5.22 \times 10^6$

accuracy of our results and qualitative connection to experiments and so proceed to a parametric study in the proceeding section.

#### 4. Results and discussion

The results section is split into two sections. The first is an investigation into the parameters present in a lubricant-infused surface, namely

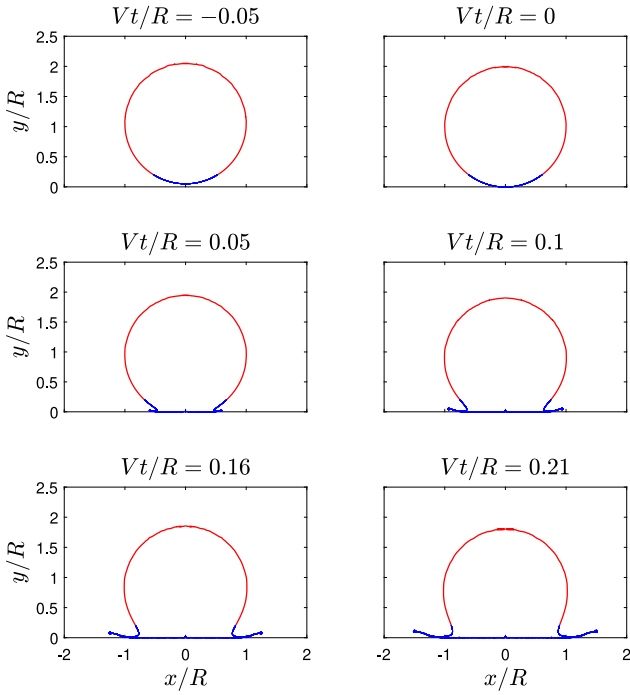


**Fig. 6.** Full free-surface solution for a droplet impact onto a surface with  $G/R = 0.01$ ,  $\mu_{LIS}/\mu_l = 30$  and  $\delta/H = 1$  at six different time instants. Impact is at  $We = 90$ . The blue line represent the solution in the refined mesh region. The surface textures and the lubricant free-surface solutions are too small to display on this scale. (For interpretation of the references to colour in this figure legend, the reader is referred to the web version of this article.)

the lubricant viscosity, the gap between the pillars and the depth of the lubricant. Lubricant-infused surfaces have many desirable features and are preferred to standard superhydrophobic, textured surfaces in many situations (Cao et al., 2016). Hence, it is important that an isolated study of the parameters pertaining to a lubricant-infused surface are investigated and results compared. Next, drawing inspiration from Yeganehdoust et al. (2021), we will compare and contrast the results against those for a superhydrophobic, textured surface to try and shed light on the key differences of the splash jet dynamics.

In order to improve the scope of our findings, results are presented in non-dimensional variables, with the liquid droplet properties as reference values. Time is also scaled such that the time  $t = 0$  corresponds to the time that the droplet bottom free-surface would reach  $y = 0$  in the absence of air cushioning. The presence of the surrounding air results in the impact being delayed slightly into positive time (Henman et al., 2021; Hicks and Purvis, 2010).

An example solution is shown in Fig. 6. This solution shows the full free-surface of the droplet in the impact. We see that the code is able to resolve the small scale features of the splash, most importantly the splash jet, which can be seen being emitted from the bottom of the droplet from time  $Vt/R = 0.05$ . A representation of the splash jet at time  $Vt/R = 0.16$  on a scale where the surface textures can be seen is shown in Fig. 7(a), together with the velocity magnitude  $|\mathbf{u}|/V$ , where  $|\mathbf{u}| = \sqrt{u^2 + v^2}$ . In what follows, a vitally important point on the splash jet is the tip, which is defined as the point of the splash jet with maximum horizontal extent. The coordinates  $(J_x, J_y)$  of this point are shown in Fig. 7(b) in non-dimensional form. Also shown is the location of the jet root  $J_r$ , a representation of the leading order wetted area of the surface, which will be examined briefly also. This point is defined as the turnover point in the free surface from the jet to the main body of the droplet.

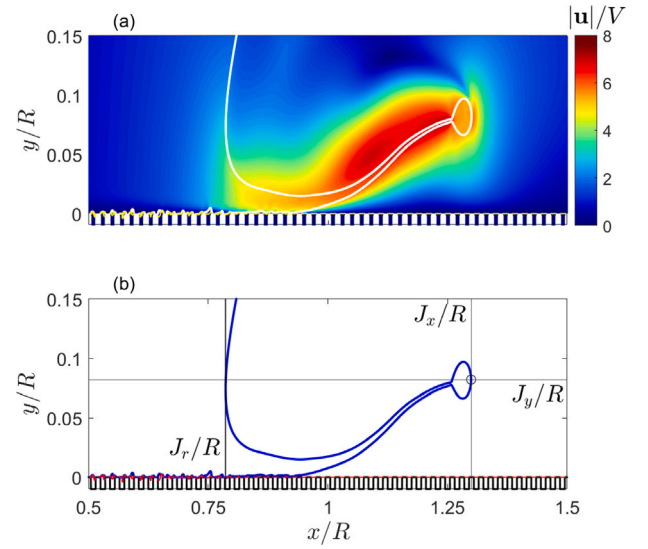


**Fig. 7.** As in Fig. 6, but at  $Vt/R = 0.16$  only and enlarged around the splash jet. (a) shows the droplet free-surface (white), the lubricant free-surface (yellow) and the velocity magnitude field (colour). (b) shows the droplet free-surface (blue), the lubricant free-surface (red) and the surface textures (black), along with the jet root location and splash jet tip coordinates. (For interpretation of the references to colour in this figure legend, the reader is referred to the web version of this article.)

#### 4.1. Lubricant-infused surfaces parameter investigation

In this section, we investigate the parameters which describe a lubricant-infused surface. Namely, they are the gap between the pillars  $G$ , the depth of the lubricant  $\delta$  and the lubricant viscosity  $\mu_{LIS}$ . Outcomes of the droplet impact are illustrated for various impact velocities. All other parameters describing the fluid flow and the geometry are held constant at the values given in Section 3.

##### 4.1.1. Effect of pillar gap variation

Firstly, in this section we consider the effect of varying the gap between the pillars  $G$ . Physically, increasing the gap between the pillars decreases the solid-fraction of the topmost surface, which for asperities filled with air can reduce the contact time of bouncing droplets (Wang et al., 2017, 2021). Here, in this section, we aim to analyse the effect pillar gap variation has on the dynamics of the splash jet when the asperities are filled with a lubricant. The lubricant viscosity and depth are kept constant at  $\mu_{LIS}/\mu_l = 30$  and  $\delta/H = 1$ , respectively. The viscosity ratio here is chosen such that our parameters are similar to Yeganehdoust et al. (2021), who model the lubricant in their simulations on Krytox GPL 101, a commonly used lubricant in lubricant-infused surfaces (Preston et al., 2017).

Fig. 8 shows free-surface solutions for both the droplet and the lubricant at  $We = 90$  and four different values of  $G/R$  from 0.01 to 0.04. In all cases here we have a distinct jet emerging from the droplet impact and this jet detaches from the surface each time. The ejection of microdrops is seen to occur at all values of  $G/R$  except for 0.01. The horizontal extent of the splash jet decreases for increased values of  $G/R$ , and this difference increases as time goes on. A video representation of the still-frame comparisons given in Fig. 8 can be found in the Supplementary Materials.

The jet root location  $J_r/R$  remains unchanged with variations of  $G/R$ , which is shown in Fig. 9 for  $We = 90$ . The jet root location compares well with the early-time Wagner theory prediction of  $2\sqrt{Vt/R}$  (Howison et al., 2005) for impact on a flat plate. The same was found to be true for  $We = 45$  and 180, for brevity this is not shown.

Time series data is shown in Fig. 10 for the aforementioned horizontal extent of the splash jet, as well as the horizontal velocity of the

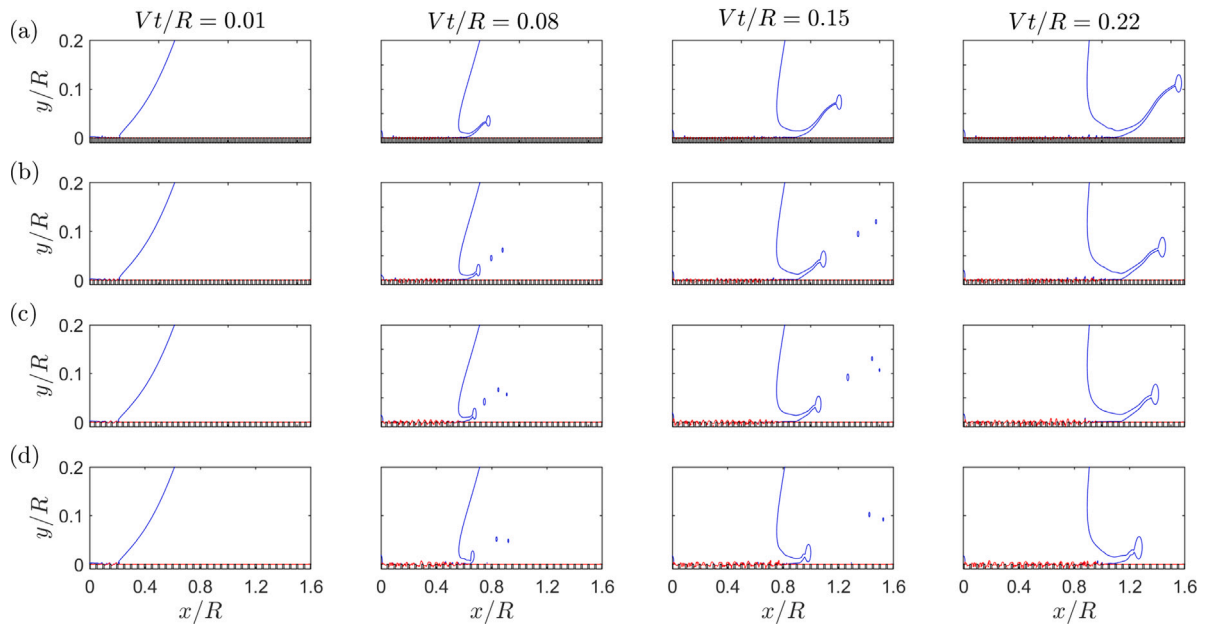


**Fig. 8.** Free-surface solutions of the droplet (blue) and the lubricant (red) at 4 equal time intervals  $Vt/R = 0.01, 0.08, 0.15, 0.22$ , with  $\mu_{LIS}/\mu_l = 30$ ,  $\delta/H = 1$  and  $We = 90$ . The pillar gap is varied, with (a)  $G/R = 0.01$ , (b)  $G/R = 0.02$ , (c)  $G/R = 0.03$  and (d)  $G/R = 0.04$ . (For interpretation of the references to colour in this figure legend, the reader is referred to the web version of this article.)

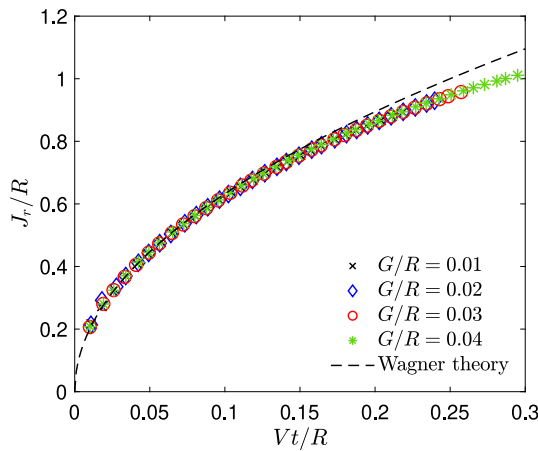


**Fig. 9.** The jet root location  $J_r/R$  for  $\mu_{LIS}/\mu_l = 30$ ,  $\delta/H = 1$  and  $We = 90$ , for  $G/R = 0.01$  (black),  $0.02$  (blue),  $0.03$  (red) and  $0.04$  (green). The dashed line shows the early-time Wagner theory prediction for the jet root location  $2\sqrt{Vt/R}$  for impact on a flat plate. (For interpretation of the references to colour in this figure legend, the reader is referred to the web version of this article.)

splash jet tip,  $J_v/V = (dJ_x/dt)/V$ , and the coordinates of the jet tip for  $G/R = 0.01$  to  $0.04$ , at  $We = 45, 90$  and  $180$ . At  $We = 45$  it can be seen that the effect of pillar gap variations is minimal. There is only a small reduction in the horizontal velocity of the jet tip as the pillar gap is increased. The jet tip coordinates show that there is an effect on the vertical position of the jet tip, but we note here that these vertical coordinates are small, and in fact the jet is attached to the surface in each case here; differences in the vertical coordinates are perhaps due to changes of curvature of the jet tip due to the definition of the jet tip in Fig. 7(b). As the Weber number is increased to  $We = 90$  (the free-surface solutions of this case are shown in Fig. 8) the effect of pillar gap variations is much more distinct. There is a clear and significant decrease in the horizontal extent of the jet, as well as the velocity and the coordinate of the splash jet tip as the pillar gap is increased from  $G/R = 0.01$  to  $G/R = 0.04$ . This is again seen for  $We = 180$ . Although a larger scatter of the data is seen in the horizontal velocity, which is due

to emission of micro droplets from the jet and the subsequent retraction of the jet due to surface tension (Culick, 1960; Taylor, 1959), as the jet forms and extends the horizontal velocity of the jet tip is significantly lower for  $G/R = 0.04$  than for  $G/R = 0.01$ . Interestingly, we see that the vertical position of the jet tip at  $We = 180$  remains the same for  $G/R = 0.02$  to  $0.04$  but is far larger for  $G/R = 0.01$ . This is, however, in keeping with the relation of larger pillar gaps resulting in a lower vertical position of the splash jet tip (see Fig. 8).

The early-time splashing behaviour is characterised into four categories: either a microdrop ejection splash (where small drops are ejected from the impact sight or from the advancing splash jet, for an example see Fig. 12(e)); a jet detachment splash (where a thin splash jet with a round rim is ejected away from the surface, see Fig. 8(a)); both microdrop ejection and jet detachment (see Fig. 8(b)) or no splash (see Fig. 12(a)). The microdrop ejection characterisation is only considered if at least one of the ejected microdrops has a diameter of at least ten grid cells (in the standard mesh this is  $5 \mu\text{m}$ ). Fig. 11 shows a summary of all early time splashing behaviour (up to  $Vt/R \approx 0.35$  in each simulation) of droplet impacts in the parameter range considered, with  $\delta/H = 1$  and  $\mu_{LIS}/\mu_l = 30$  fixed and  $G/R$  and  $We$  varied. Below  $We \approx 79$ , no splash is observed for all surfaces considered. As  $We$  increases to  $135$ , the behaviour transitions to a splash with both microdrop ejection and jet detachment characteristics, with this splashing behaviour seen first at larger values of  $G/R$ , suggesting that despite larger values of  $G/R$  having a suppressing effect on the horizontal extent of the splash jet, it may promote microdrop ejection. This behaviour then continues up until  $We \approx 202$ , where at  $G/R = 0.4$  the presence of a distinct jet detachment ceases to be seen, perhaps due to larger velocities and asperities allowing more lubricant to leave the surface and influence the advancing of the splash jet (see Supplementary Materials for a video of this case).

The results here show that the pillar gap  $G$  can be an important quantity in reducing the splash jet's horizontal extent and the velocity and coordinate of the jet tip, but has no effect on the jet root location. These three metrics suggest that the magnitude of a jet detachment splash can be suppressed by increasing the gaps between pillars on a lubricant-infused surface. There is a limited number of experimental studies on high-speed droplet impact on lubricant-infused surfaces, and an absence of such that consider the effect of varying the distance

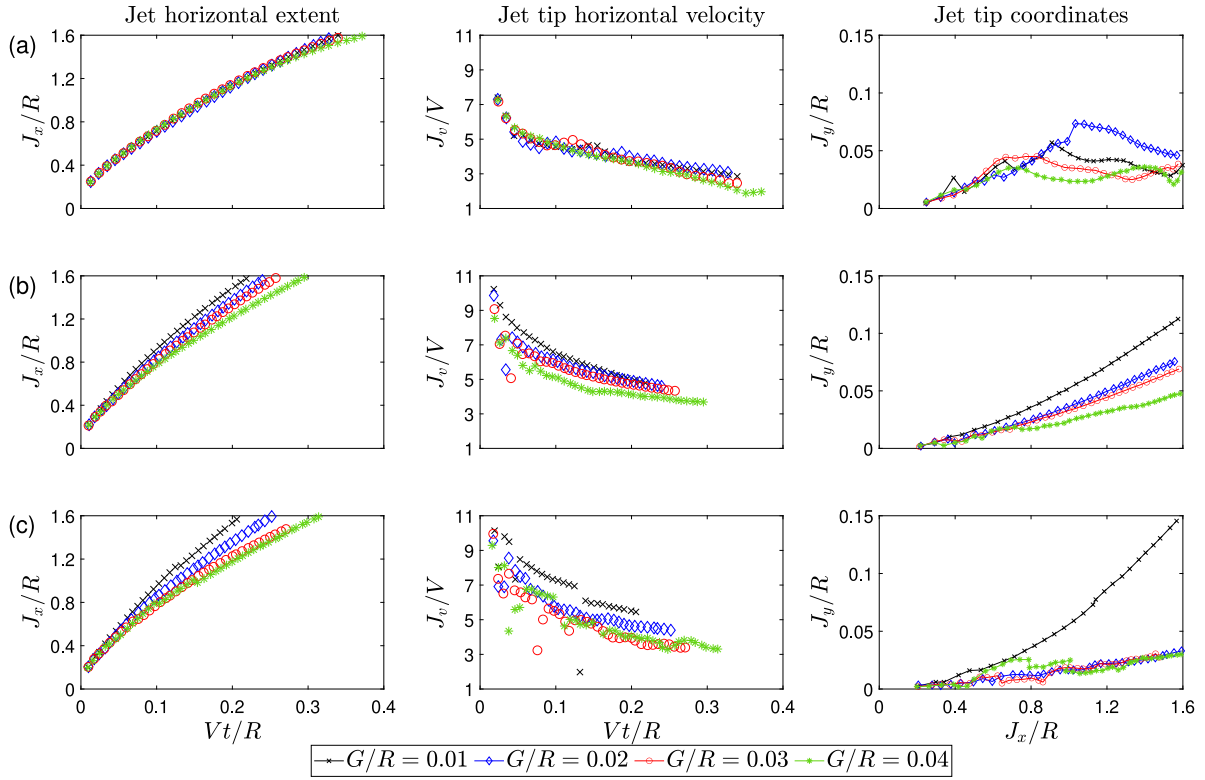


**Fig. 10.** Time series data for the jet horizontal extent (left) and the jet tip horizontal velocity (middle) as well as the jet tip coordinates (right), with  $\mu_{LIS}/\mu_l = 30$ ,  $\delta/H = 1$  and  $G/R = 0.01$  (black), 0.02 (blue), 0.03 (red), 0.04 (green) for row (a)  $We = 45$ , (b)  $We = 90$  and (c)  $We = 180$ . (For interpretation of the references to colour in this figure legend, the reader is referred to the web version of this article.)

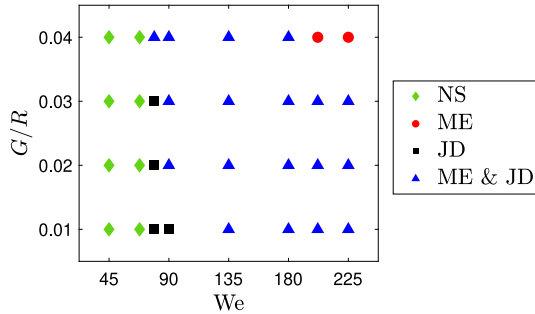


**Fig. 11.** Early time splashing behaviour of droplet impacts onto surfaces with  $\delta/H = 1$  and  $\mu_{LIS}/\mu_l = 30$ . The different behaviours are defined as either no splash (NS), microdrop ejection (ME) or jet detachment (JD).

between the asperities of the surface. One possible mechanism of the suppressed splash dynamics for larger values of  $G$  could be the effect the lubricant has in making the surface effectively rough. Larger fluid filled cavities are susceptible to greater deformation from flow across them (Asmolov et al., 2020), thus surfaces with larger values of  $G$  deform more as the droplet impacts and subsequently spreads over it. Significant surface roughness is known to inhibit corona splashing (Latka et al., 2012), which is related to jet detachment, and so is then consistent with our results.

#### 4.1.2. Effect of lubricant depth variation

Next we turn our attention to the initial depth  $\delta$  of the lubricant present. The initial depth of the lubricant may not necessarily be something that is designed on purpose, but instead something that happens over time (Peppou-Chapman et al., 2020). For example, a lubricant-infused surface may begin life with a lubricant level that is

slightly above the asperities ( $\delta/H > 1$ ), but after successive liquid impacts or droplet sliding, lubricant depletion may occur (Laney et al., 2021; Smith et al., 2013), eventually resulting in a lubricant level below the asperities ( $\delta/H < 1$ ). The lubricant depth can be engineered however, by using a spin coating method for example (Muschi et al., 2018). In this section, we aim to investigate the dynamics of a droplet impact for different lubricant levels  $\delta$ . Again, we will keep the viscosity of the lubricant constant at  $\mu_{LIS}/\mu_l = 30$  and we will choose the surface textures to be all equal such that  $G/R = 0.01$ .

Fig. 12 shows free-surface solutions for both the droplet and the lubricant at  $We = 90$  and five different values of  $\delta/H$  from 0 to 2. The droplet impact dynamics illustrated by Fig. 12 are similar to that seen in Fig. 10, the splash jet clearly emerges and extends horizontally as time goes on for all values of  $\delta/H$ ; however there are some key and interesting outcomes as  $\delta/H$  is varied. When  $\delta/H = 0$ , the surface is no longer a lubricant-infused surface and is in fact a textured surface. The splash jet spreads along the surface without detaching, exhibiting no splashing behaviour whatsoever. Almost identical behaviour is seen for  $\delta/H = 0.5$ , showing that a small amount of lubricant present has little effect. The solution for  $\delta/H = 1$  is the same as in Fig. 10(a), showing that once the lubricant is at a depth large enough to affect the droplet impact it results in the splash jet detaching from the surface and having a larger horizontal extent. Here, a small increase in the depth to  $\delta/H = 1.5$  has little effect. When  $\delta/H = 2$ , the splash jet is clearly suppressed, being expelled along the liquid surface as opposed to up and away from it. A video representation of the still-frame comparisons given in Fig. 12 can be found in the Supplementary Materials.

As in the previous section, the jet root location is virtually unaffected by variations in the initial lubricant depth. The graph of jet root location against time is similar to Fig. 9 and can be found in the Supplementary Materials. The same is true at  $We = 45$  and 180.

The time series data for the splash jet horizontal extent and tip velocity, as well as the splash jet tip coordinates, for variations in  $\delta/H$

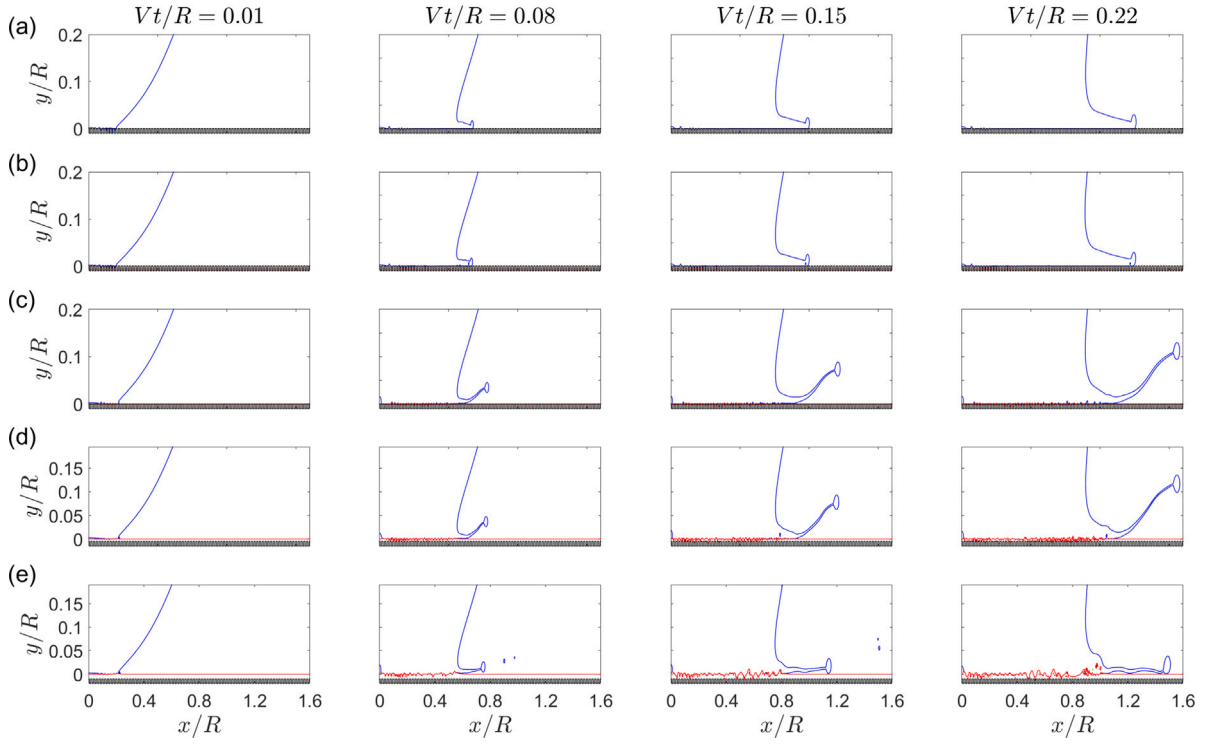


**Fig. 12.** Free-surface solutions of the droplet (blue) and the lubricant (red) at 4 equal time intervals  $Vt/R = 0.01, 0.08, 0.15, 0.22$ , with  $\mu_{LIS}/\mu_l = 30$ ,  $G/R = 0.01$  and  $We = 90$ . The lubricant depth is varied, with (a)  $\delta/H = 0$ , (b)  $\delta/H = 0.5$ , (c)  $\delta/H = 1$ , (d)  $\delta/H = 1.5$  and (e)  $\delta/H = 2$ . (For interpretation of the references to colour in this figure legend, the reader is referred to the web version of this article.)

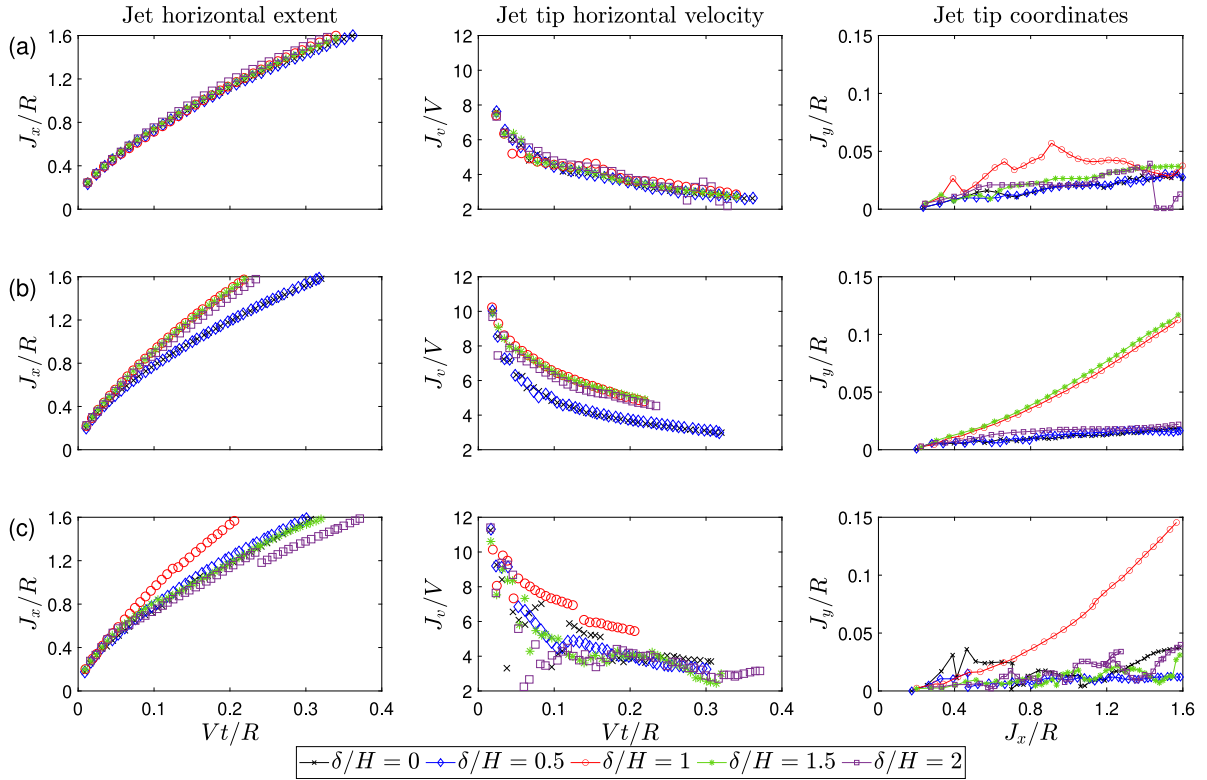


**Fig. 13.** Time series data for the jet horizontal extent (left), the jet tip horizontal velocity (middle), as well as the jet tip coordinates (right), with  $\mu_{LIS}/\mu_l = 30$ ,  $G/R = 0.01$  and  $\delta/H = 0$  (black), 0.5 (blue), 1 (red), 1.5 (green), 2 (purple) for row (a)  $We = 45$ , (b)  $We = 90$  and (c)  $We = 180$ . (For interpretation of the references to colour in this figure legend, the reader is referred to the web version of this article.)

is shown in Fig. 13. As in the previous section, at  $We = 45$ , varying  $\delta/H$  has a minimal effect on the three splash metrics considered here.

At  $We = 90$  we have the dynamics that are explained above. The horizontal extent of the splash jet and velocity of the tip are significantly

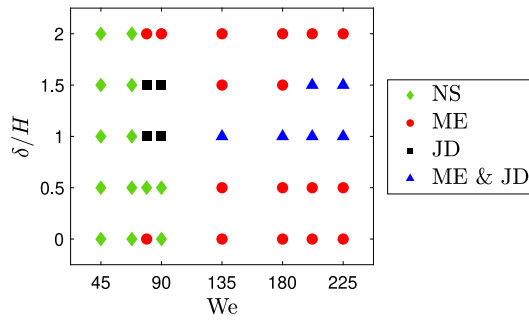


Fig. 14. Early time splashing behaviour of droplet impacts onto surfaces with  $G/R = 0.01$  and  $\mu_{LIS}/\mu_l = 30$ . The different behaviours are defined as either no splash (NS), microdrop ejection (ME) or jet detachment (JD).

reduced for  $\delta/H = 0$  and  $0.5$  compared to larger values of  $\delta/H$ . The vertical coordinate of the splash jet tip behaves similarly, except for when  $\delta/H = 2$ , where the viscous film has a suppressing effect. At a higher Weber number,  $We = 90$ , the dynamics are slightly different: specifically the suppressing effect on the splash jet for surfaces with  $\delta/H > 1$  is much more profound. The horizontal extent of the splash jet is lower for all time for the  $\delta/H > 1$  cases than it is for the  $\delta/H < 1$  cases, unlike for  $We = 90$ . The horizontal velocities and vertical positions of the jet tip are also reduced to a similar level. Again, we see greater horizontal extent of the jet and velocity and vertical positions of the jet tip for the level case of  $\delta/H = 1$ .

As in the previous section, a parametric diagram (Fig. 14) summarises the early time splashing behaviour for various values of  $\delta/H$  and  $We$ , with  $G/R = 0.01$  and  $\mu_{LIS}/\mu_l = 30$ . Again, below  $We \approx 79$ , no splashing is observed. However, now, no splashing is observed up until  $We = 90$  for  $\delta/H < 1$ . After  $We \approx 90$ , the different outcomes are split above and below  $\delta/H = 1$ . At  $\delta/H = 1$ , the droplet impact exhibits both microdrop ejection and jet detachment splashing past  $We \approx 90$ , whereas above and below  $\delta/H = 1$ , the droplet impact exhibits only microdrop ejection splashing behaviour, except for higher  $We$  where we begin to see jet detachment splashing occurring at  $\delta/H = 1.5$ .

Muschi et al. (2018) considered the effect of varying the lubricant thickness in a lubricant-infused surface. In their study, at  $We = 66$ , they show that in the early stages of droplet impact the droplet spreads slower on a porous surface with no lubricant present than it does on a surface with the lubricant slightly above the asperities, which agrees with our results at  $We = 45$  and  $90$  somewhat over the small time scales considered here. Our results point towards an interesting transition as the depth of the lubricant  $\delta$  is increased from zero. When the surface of the lubricant is below the level of the asperities of the solid surface, the latter surface behaves like a textured surface, with the droplet able to penetrate much further into the surface and more space is available for the air underneath the tip of the advancing jet to drain into, suppressing the jet detachment splash (Latka et al., 2012; Riboux and Gordillo, 2014; Xu et al., 2007). As the depth is increased however to the level of the asperities the splash magnitude becomes rather large (only lubricant depths which are above the asperities are considered in Muschi et al. (2018)). In this case, the air is no longer able to drain from underneath the advancing jet tip and the disturbances from the deformation in the lubricant result in the splash jet being ejected away from the surface. As the depth is increased further, above the asperities, the splashing can be seen to become suppressed again. Thin layers of viscous fluid could have connection to soft solids, which are known to have a suppressing effect on droplet splashing (Howland et al., 2016). This points towards a non-monotonic relationship in the level of splashing seen as the depth of the lubricant is varied. The magnitude of the splash is also seen to be dependent on the Weber number, by Fig. 13, with the magnitude of the splash particularly affected by the Weber number when the lubricant surface is above the

asperities. Of course, interesting cases where the lubricant level is a small amount below or above the asperities would ideally be considered here also, but to ensure numerical accuracy the mesh would need to be refined to a level beyond our computational capabilities. Our results here nevertheless do suggest a broad and general trend.

#### 4.1.3. Effect of viscosity ratio variation

Our final parameter of interest will be the viscosity of the lubricant. This is perhaps the most commonly investigated parameter in experimental studies (Kim and Rothstein, 2016; Preston et al., 2017). In practise, the viscosity of the lubricant used varies drastically (Peppou-Chapman et al., 2020), with magnitudes ranging from  $O(10^{-2}) - O(1)$  Pa s for the Krytox series of lubricants, which for a water droplet gives viscosity ratios in the range  $\mu_{LIS}/\mu_l = O(1) - O(10^3)$ . As well as the previous case of  $\mu_{LIS}/\mu_l = 30$ , which was based on the Krytox 101 lubricant, we will now consider other values of the viscosity ratio, choosing a range which represents the orders of magnitude range above. Here, the depth of the lubricant and the gap between the pillars will be held constant, with  $\delta/H = 1$  and  $G/R = 0.01$ .

Free surface solutions for the droplet and the lubricant at  $We = 90$  are shown in Fig. 15, for  $\mu_{LIS}/\mu_l = 2, 10, 30, 100, 500$  and  $1500$ . Again we see a number of different outcomes of the splash jet. Starting with  $\mu_{LIS}/\mu_l = 1500$ , we can see from the solution at  $Vt/R = 0.08$  that the splash jet is ejected at a small angle, almost along the surface. As time increases the jet continues to extend along the surface and does make contact with the surface again, resulting in a break-up of the jet (although this separated fluid is then absorbed by the spreading jet at later times). Decreasing the viscosity ratio to  $\mu_{LIS}/\mu_l = 500$  and  $\mu_{LIS}/\mu_l = 100$  results in the jet being ejected at a much larger angle, with results that are almost identical to that of the previous results with viscosity ratio of  $\mu_{LIS}/\mu_l = 30$ , which is repeated here for clarity. Decreasing the viscosity ratio further to  $\mu_{LIS}/\mu_l = 10$  we can see again at early times that the jet is ejected at an angle similar to those seen in the previous two cases, but this time much more of the jet is still attached to the surface, with atomisation also occurring. Both these attributes contribute to the horizontal extent of the jet being reduced compared to previous cases. Finally, for a relatively low viscosity ratio of  $\mu_{LIS}/\mu_l = 2$ , the lubricant is able to deform more and allows the droplet to penetrate deeper during impact. This results in the jet being ejected at a small angle and being of comparatively small extent. As time advances, the jet remains comparatively small in both horizontal and vertical extent. A video representation of the still-frame comparisons given in Fig. 15, except  $\mu_{LIS}/\mu_l = 100$ , can be found in the Supplementary Materials.

As in the previous two sections, the jet root location is virtually unaffected by variations in the viscosity ratio. The graph of jet root location against time at  $We = 90$  is similar to Fig. 9 and can be found in the Supplementary Materials. The same is true at  $We = 45$  and  $180$ .

Time series data for horizontal extend of the splash jet and the velocity of the jet tip, as well as the jet tip coordinates are shown in Fig. 16 and compared to the same data found from impacts at  $We = 45$  and  $We = 180$ . At  $We = 45$ , as for the previous two parameters we studied, the changes in the horizontal extent of the jet and velocity of the tip are relatively small as we vary the viscosity ratio. There would appear to be some difference here in the jet tip coordinates, with a gradual decrease in vertical extent seen as  $\mu_{LIS}/\mu_l$  decreases from  $500$  to  $2$ , and then also a decrease as we increase it from  $500$  to  $1500$ . Time series data for the free-surface results at  $We = 90$  discussed above are also shown, and highlight similar trends to the  $We = 45$  case for the three metrics considered, a gradual decrease in magnitude as the viscosity ratio decreases from  $500$  to  $2$  and then a decrease also as it is increased from  $500$  to  $1500$ . However this time the results for  $\mu_{LIS}/\mu_l = 500, 100$  and  $30$  are very similar and the decrease in magnitude seen from the increase of the viscosity ratio from  $500$  to  $1500$  is much more profound now, compared with that at  $We = 45$ . At  $We = 180$ , we can see that the results for  $\mu_{LIS}/\mu_l = 500$  are now

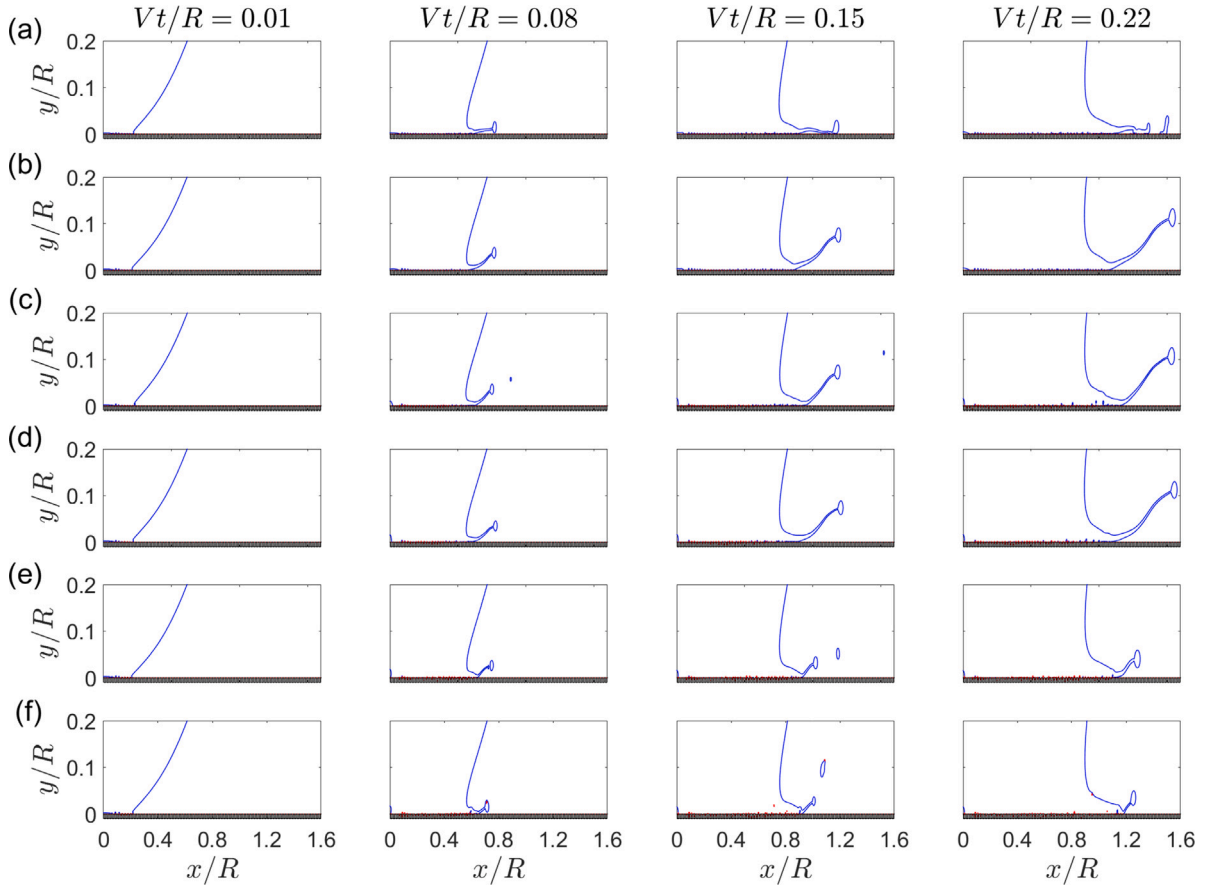


**Fig. 15.** Free-surface solutions of the droplet (blue) and the lubricant (red) at 4 equal time intervals  $Vt/R = 0.01, 0.08, 0.15, 0.22$ , with  $\delta/H = 1$ ,  $G/R = 0.01$  and  $We = 90$ . The lubricant viscosity is varied, with (a)  $\mu_{LIS}/\mu_l = 1500$ , (b)  $\mu_{LIS}/\mu_l = 500$ , (c)  $\mu_{LIS}/\mu_l = 100$  (d)  $\mu_{LIS}/\mu_l = 30$ , (e)  $\mu_{LIS}/\mu_l = 10$  and (f)  $\mu_{LIS}/\mu_l = 2$ . (For interpretation of the references to colour in this figure legend, the reader is referred to the web version of this article.)

below those of  $\mu_{LIS}/\mu_l = 30$  and  $100$ , which are again almost identical, for all three metrics. Hence, these time series data shown in Fig. 16 would point again towards a non-monotonic relationship between the viscosity ratio and the jet dynamics and subsequent splashing. For a larger viscosity ratio, the fluid between the asperities is less able to deform, thus the surface itself would behave more like a flat rigid surface, on which it is harder for a droplet to splash than is the case on a rough surface (Xu et al., 2007). However, as the viscosity ratio is reduced further, we observe a transition of the dynamics and the magnitude of the splash starts to decrease. As the viscosity ratio decreases, the droplet fluid is more able to penetrate deeper into the asperities of the surface, which results in the surface behaving more like a textured surface (in which the asperities would be filled with air, which obviously has a much smaller viscosity than the droplet fluid), which also has splash suppressant qualities. These dynamics are also dependent on the impact Weber number. More specifically, it would appear that the decrease in splash magnitude seen for very large viscosity ratios is more profound at higher Weber numbers.

Fig. 17 summarises the early time splashing behaviour for these parameters. Interestingly, unlike in the previous two investigated parameters, for values above  $\mu_{LIS}/\mu_l \approx 100$ , a jet detachment splash is observed for low  $We$ . The phase diagram here is, mainly, split into four regions. At low  $We$  and below  $\mu_{LIS}/\mu_l \approx 500$ , no splashing behaviour is exhibited. At high viscosity ratios, below  $We \approx 135$  only jet detachment splashing occurs and at  $\mu_{LIS}/\mu_l = 2$ , above  $We \approx 45$ , only microdrop ejection splashing occurs (except for at  $We = 202$ ). The rest of the phase diagram shows both microdrop ejection and jet detachment splashing.

Spreading and retracting dynamics of droplet impacts with lubricant-infused surfaces of varying viscosities were examined experimentally

in Kim and Rothstein (2016), with viscosity ratios ranging from  $0.8$  to  $16.7$ . They found that, in contrast to our results, decreasing the surface lubricant viscosity led to a faster spreading and retracting rate of droplet impacts. However, it should be noted that in their study only droplet impacts of relatively low velocity were considered (up to  $1.9 \text{ ms}^{-1}$ ) and that the overall spreading and retracting dynamics happen over a much longer time scale than that considered in our study. In our study, a  $1 \text{ mm}$  radius water droplet impact at  $We = 45$  corresponds to an impact velocity of  $V = 1.81 \text{ ms}^{-1}$ , at the upper end of the experimental range in Kim and Rothstein (2016), and Fig. 16 shows minimal variation in the horizontal extent of the splash jet. At higher  $We$ , the horizontal extent of the splash jet decreases noticeably (over the range of viscosity ratios in the experimental study (Kim and Rothstein, 2016)). And so we conclude that at lower impact velocities, where the deformation of the lubricant itself is minimal, droplets will spread faster for lower viscosity lubricants, due to larger slippage occurring at the lubricant-droplet interface. But at higher impact velocity, where the lubricant can deform and allow the droplet to penetrate into the asperities, the splash jet that is emitted extends at a lower velocity for lower lubricant viscosities. As the viscosity ratio becomes  $O(100)$ , this trend does begin to change somewhat, suggesting new dynamics that need to be considered.

#### 4.2. Comparison of lubricant-infused surfaces and textured, superhydrophobic surfaces

The purpose of this section is to compare the results for lubricant-infused surfaces, given above, to those of textured, superhydrophobic surfaces, where there is no lubricant present and the surface cavities

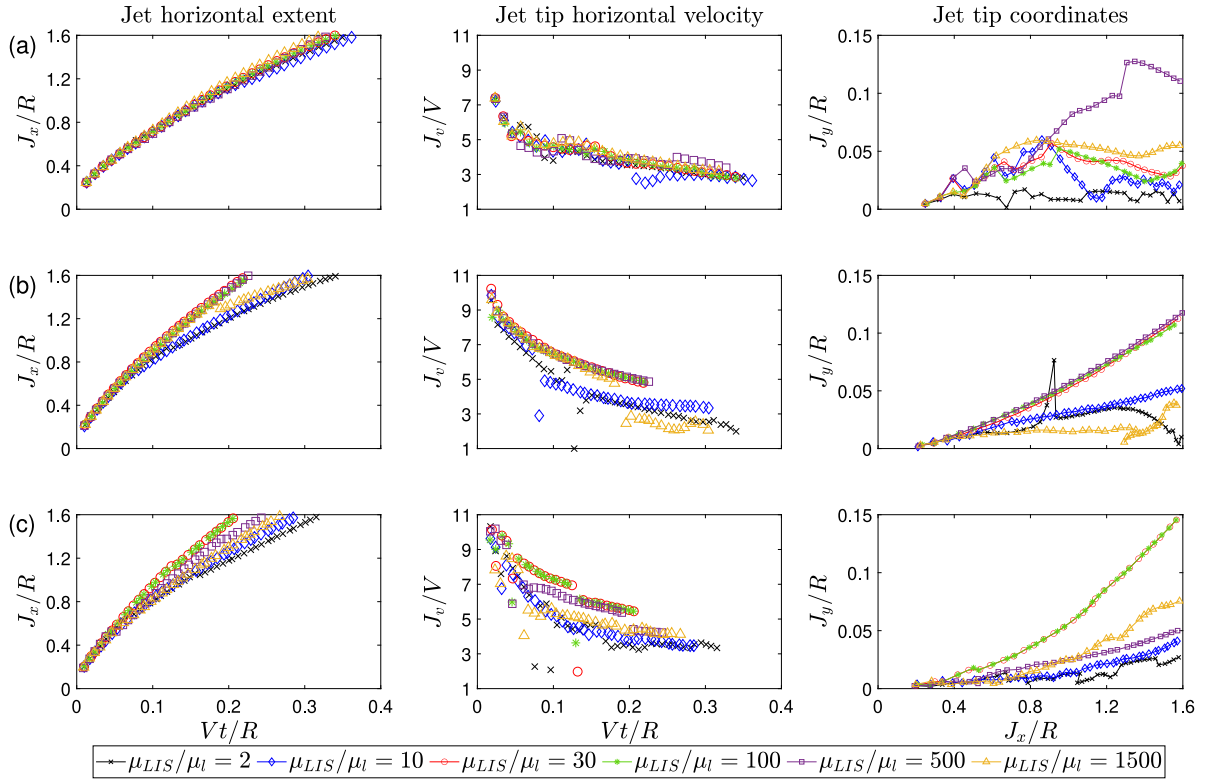


**Fig. 16.** Time series data for the jet horizontal extent (left) and the jet tip horizontal velocity (middle), as well as the jet tip coordinates (right), with  $\delta/H = 1$ ,  $G/R = 0.01$  and  $\mu_{LIS}/\mu_l = 2$  (black), 10 (blue), 30 (red), 100 (green), 500 (purple), 1500 (orange) for row (a)  $We = 45$ , (b)  $We = 90$  and (c)  $We = 180$ . (For interpretation of the references to colour in this figure legend, the reader is referred to the web version of this article.)

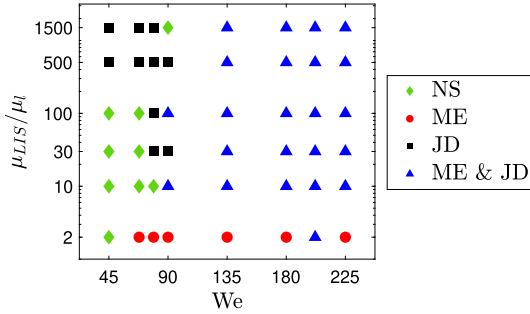


**Fig. 17.** Early time splashing behaviour of droplet impacts onto surfaces with  $G/R = 0.01$  and  $\delta/H = 1$ . The different behaviours are defined as either no splash (NS), microdrop ejection (ME) or jet detachment (JD).

are filled with air instead (this is equivalent to setting  $\delta/H = 0$  in the modelling). While lubricant-infused surfaces have benefits in their own right, textured, superhydrophobic surfaces also have many benefits, some of which are the same as lubricant-infused surfaces, some not (Mousavi and Pitchumani, 2022; Stoddard et al., 2022; Zhang et al., 2020).

In this section we compare the splash jet dynamics of droplet impacts onto a lubricant-infused surface with viscosity ratio  $\mu_{LIS}/\mu_l = 30$  and a lubricant depth of equal size to the asperities of the surface ( $\delta/H = 1$ ), to that of a textured, superhydrophobic surface ( $\delta/H = 0$ ). We consider and compare different impact velocities and variations in the pillar gap  $G/R$ .

Fig. 18 shows a comparison of the droplet free-surface solutions for impacts onto a lubricant-infused surface and a textured surface, both with a pillar gap of  $G/R = 0.01$ , at  $We = 45$ , 90 and 180. At  $We = 45$ , although marginal, it is quite clear that the horizontal

extent of the splash jet is reduced on a textured surface compared to a lubricant-infused surface. This is also seen at  $We = 90$ , and much more profound this time. Not only is the horizontal extent less for a textured surface, the vertical extent is also, with the jet remaining attached to the substrate whereas it is detached on a lubricant-infused surface. At  $We = 180$ , we begin to see a significant amount of atomisation and breakup of the jet, and at early times ( $Vt/R = 0.07$ ) the jet is detached from the surface in both cases. However, as time advances the jet on the textured surface is attached to the surface and has a horizontal and vertical extent significantly less than for the lubricant-infused surface.

In order to explore the effect of different pillar gap sizes and the influence of the impact velocity, for brevity a single metric will be considered, which is the time taken for tip of the splash jet to reach a specified point on the  $x$ -axis. Explicitly, this is given in non-dimensional terms as

$$T_i = \left\{ \frac{Vt}{R}, \text{ such that } \frac{J_x}{R} = c \right\} \quad (7)$$

for some value  $c$  and  $i = LIS$  for a lubricant-infused surface whereas  $i = SHS$  for a textured, superhydrophobic surface. For our study we will consider  $c = 1.6$ , which corresponds to a point towards the end of the refined mesh region in the simulations. The parameter  $T_i$  will be evaluated at a number of different pillar gaps  $G/R$  and Weber numbers. Fig. 19 shows the difference between the time parameters for a lubricant-infused surface and a textured, superhydrophobic surface  $T_{SHS} - T_{LIS}$  plotted against pillar gap  $G/R$ . This figure shows that, as shown in Fig. 18, the jet tip advances slower on the textured surface compared to the lubricant-infused surface for  $G/R = 0.01$ , and so the difference  $T_{SHS} - T_{LIS} > 0$  for all three Weber numbers considered. At each Weber number, when the pillar gap  $G/R$  is increased, the difference  $T_{SHS} - T_{LIS}$  decreases (except for  $We = 45$  from  $G/R = 0.01$  to 0.02, where it increases slightly), where eventually for  $G/R = 0.04$  we have  $T_{SHS} - T_{LIS} \lesssim 0$ , for all three Weber numbers, illustrating that when the pillar gap is raised sufficiently, the jet extends slower on a lubricant-infused surface than on a textured one.

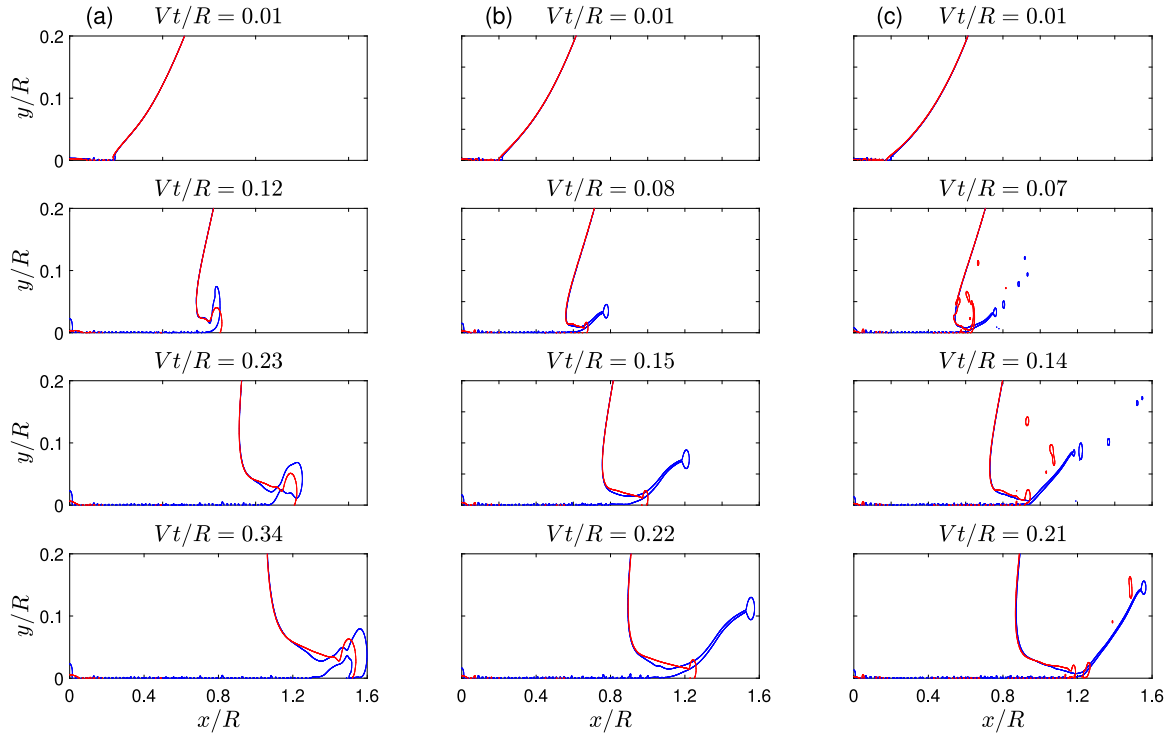


**Fig. 18.** Comparison of free-surface solutions for droplet impacts onto lubricant-infused surfaces (blue) and textured, superhydrophobic surfaces (red). Results are shown for  $\mu_{LIS}/\mu_l = 30$  and  $\delta/H = 1$  (lubricant-infused surface) and  $\delta/H = 0$  (textured surface), with  $G/R = 0.01$  and  $We = 45$  (column (a)),  $We = 90$  (b) and  $We = 180$  (c). Results are shown for  $y/R > 0$  only, and free-surface solutions for the lubricant are not shown. (For interpretation of the references to colour in this figure legend, the reader is referred to the web version of this article.)

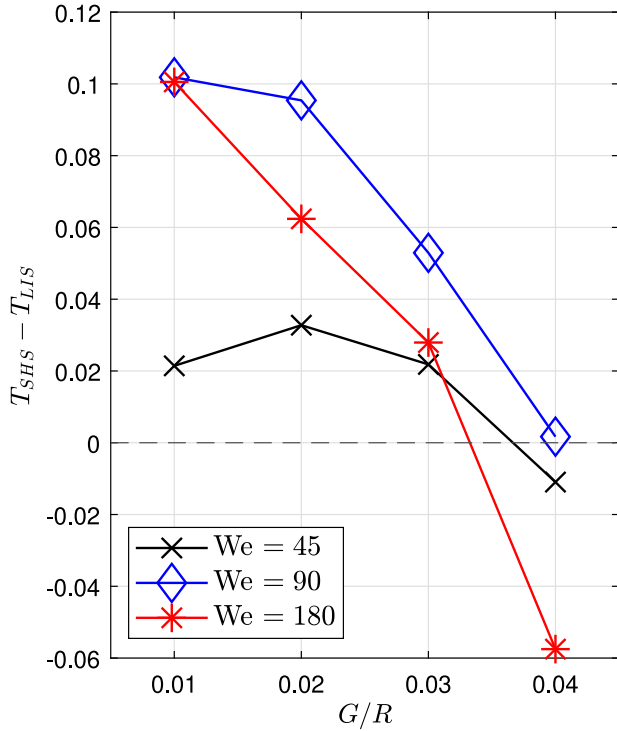


**Fig. 19.** The difference between the time parameters  $T_{SHS}$  and  $T_{LIS}$  against pillar gap  $G/R$  for  $c = 1.6$ , at  $We = 45$  (black),  $We = 90$  (blue) and  $We = 180$  (red). For the lubricant-infused surface  $\mu_{LIS}/\mu_l = 30$  and  $\delta/H = 1$ . (For interpretation of the references to colour in this figure legend, the reader is referred to the web version of this article.)

## 5. Conclusions

In this paper we have explored the solutions to a computational model of droplet impact on to textured and lubricant-infused surfaces. The textured surface was modelled as an array of rectangular asperities in an otherwise flat, rigid surface, with the asperities filled up to a certain depth with lubricant. We systematically investigated parameters of the surface, namely the distance between the asperities, the depth of the lubricant and the lubricant viscosity.

First, we compared results for variations in the parameters pertaining to a lubricant-infused surface. For variations of any of the surface parameters there was no change in the jet root location. All variations in the early-time dynamics were seen in the thin splash jet ejected at impact. It was found that on increasing the distance between the surface asperities, the splash jet extent and tip velocity were reduced, effects which are more profound at higher impact velocity. The depth of the lubricant was identified to have a suppressing effect on the splash jet extent and velocity when the depth of the lubricant is above or below the asperities, compared to when the lubricant depth is level with the asperities. When varying the viscosity of the lubricant, a non-monotonic relationship is also apparent. As the viscosity ratio is increased from an order unity value, the extent and the tip velocity of the splash jet are increased, due to less penetration of the droplet into the asperities. Then, as the viscosity ratio becomes very large, the extent and tip velocity of the splash jet start to decrease again, as the surface becomes flatter due to less deformability of the lubricant. The suppressing effect on the splash jet for large viscosity ratios is more profound at higher impact velocity. For each parameter, a rough phase field diagram of different early time splashing behaviours (jet detachment or microdrop ejection splashing) was presented for variations in the parameter of interest and the Weber number. When considering the pillar spacing, it was seen that the splashing behaviour transitioned from no splash to

both jet detachment and microdrop ejection splashing relatively quickly when increasing the Weber number, with both behaviours being seen at a lower Weber number when the pillar spacing was larger, suggesting that larger pillar spacing promotes microdrop ejection splashing while suppressing jet detachment splashing. When the pillar spacing was larger and the Weber number was sufficiently high, the jet detachment splash was completely suppressed. For variations in the lubricant depth it was found that depths of lubricant above and below the asperities had a suppressing effect on the jet detachment splash, which eventually waned slightly for lubricant levels above the asperities as the Weber number increased. When considering the viscosity ratio, we broadly saw four regions. At low Weber number and viscosity ratio, no splash was observed, while for low Weber numbers and large viscosity ratios, a jet detachment splash was observed. At very low viscosity ratio, microdrop ejection splashing was observed for most Weber numbers considered. Finally for large Weber numbers and large viscosity ratios, both jet detachment and microdrop ejection splashing occurred.

Next, we compared the results for lubricant-infused surfaces to those of textured, superhydrophobic surfaces, where no lubricant is present. It was found that as the distance between the surface asperities was increased, the extent of the splash jet eventually went from being larger on the lubricant-infused surfaces, compared to the textured, superhydrophobic surfaces, to smaller (or similar) values.

The aim of this numerical study was to explore parameters and scales unavailable to analytical methods and which have received only a small amount of interest experimentally. We hope that our idealised two-dimensional model can be used as a qualitative measure of the parameters pertaining to lubricant-infused surfaces and hopefully suggest further avenues for experimental and analytical work. For example the response of the splash jet in certain situations (e.g. in Fig. 8) perhaps indicates that a form of boundary-layer separation could usefully be analysed; again, an analytical study of two-fluid flow over asperities could shed further light here. With respect to the present study, further extensions would ideally be focused around a fully resolved three-dimensional solution of the splash jet on textured and lubricant-infused surfaces and also perhaps longer time scales to build a fuller picture of the impact dynamics.

#### CRedit authorship contribution statement

**Nathaniel I.J. Henman:** Conceptualization, Methodology, Software, Validation, Formal analysis, Writing – original draft, Visualization. **Frank T. Smith:** Conceptualization, Writing – review & editing, Supervision, Funding acquisition. **Manish K. Tiwari:** Conceptualization, Writing – review & editing, Supervision, Funding acquisition.

#### Declaration of competing interest

The authors declare that they have no known competing financial interests or personal relationships that could have appeared to influence the work reported in this paper.

#### Data availability

Data will be made available on request.

#### Acknowledgements

N.I.J.H. thanks UCL, United Kingdom for financial support and is very grateful for the use of the UCL Kathleen High Performance Computing Facility and associated support services. F.T.S. thanks EPSRC, United Kingdom and UCL, United Kingdom for continued support, including Grant Nos. EP/R511638/1, GR/T11364/01, EP/G501831/1, EP/H501665/1, and EP/K032208/1. M.K.T. acknowledges the funding from the European Union's Horizon 2020 Research and Innovation programme under the European Research Council (ERC) grant 714712 (NICEDROPS) and the Royal Society Wolfson Fellowship, United Kingdom. We would also like to thank the anonymous referees for their helpful and interesting comments, which helped improve this manuscript.

#### Appendix A. Supplementary data

Supplementary material related to this article can be found online at <https://doi.org/10.1016/j.ijmultiphaseflow.2023.104398>.

#### References

- Antonini, C., Innocenti, M., Horn, T., Marengo, M., Amirfazli, A., 2011. Understanding the effect of superhydrophobic coatings on energy reduction in anti-icing systems. *Cold Reg. Sci. Technol.* 67 (1), 58–67.
- Asmolov, E.S., Nizkaya, T.V., Vinogradova, O.I., 2020. Flow-driven collapse of lubricant-infused surfaces. *J. Fluid Mech.* 901, A34.
- Biroun, M.H., Haworth, L., Agrawal, P., Orme, B., McHale, G., Torun, H., Rahmati, M., Fu, Y., 2021. Surface acoustic waves to control droplet impact onto superhydrophobic and slippery liquid-infused porous surfaces. *ACS Appl. Mater. Interfaces* 13 (38), 46076–46087.
- Bohn, H.F., Federle, W., 2004. Insect aquaplaning: nepenthes pitcher plants capture prey with the peristome, a fully wettable water-lubricated anisotropic surface. *Proc. Natl. Acad. Sci. USA* 101 (39), 14138–14143.
- Brackbill, J., Kothe, D., Zemach, C., 1992. A continuum method for modeling surface tension. *J. Comput. Phys.* 100 (2), 335–354.
- Cao, M., Guo, D., Yu, C., Li, K., Liu, M., Jiang, L., 2016. Water-repellent properties of superhydrophobic and lubricant-infused slippery surfaces: A brief study on the functions and applications. *ACS Appl. Mater. Interfaces* 8 (6), 3615–3623.
- Cimpeanu, R., Moore, M.R., 2018. Early-time jet formation in liquid-liquid impact problems: theory and simulations. *J. Fluid Mech.* 856, 764–796.
- Culick, F.E.C., 1960. Comments on a ruptured soap film. *J. Appl. Phys.* 31 (6), 1128–1129.
- Delele, M.A., Nuytens, D., Duga, A.T., Ambaw, A., Lebeau, F., Nicolai, B.M., Verboven, P., 2016. Predicting the dynamic impact behaviour of spray droplets on flat plant surfaces. *Soft Matter* 12, 7195–7211.
- Elliott, J.W., Smith, F.T., 2017. Ice formation on a smooth or rough cold surface due to the impact of a supercooled water droplet. *J. Eng. Math.* 102, 35–64.
- Ellis, A.S., Smith, F.T., White, A.H., 2011. Droplet impact on to a rough surface. *Q. J. Mech. Appl. Math.* 64 (2), 107–139.
- Fauchais, P., Vardelle, A., Vardelle, M., Fukumoto, M., 2004. Knowledge concerning splat formation: An invited review. *J. Therm. Spray Tech.* 13, 337–360.
- Henman, N.I.J., Smith, F.T., Tiwari, M.K., 2021. Pre-impact dynamics of a droplet impinging on a deformable surface. *Phys. Fluids* 33 (9), 092119.
- Hicks, P.D., 2022. Violent droplet impacts with non-flat surfaces. *J. Fluid Mech.* 939, A31.
- Hicks, P.D., Purvis, R., 2010. Air cushioning and bubble entrapment in three-dimensional droplet impacts. *J. Fluid Mech.* 649, 135–163.
- Howison, S.D., Ockendon, J.R., Oliver, J.M., Purvis, R., Smith, F.T., 2005. Droplet impact on a thin fluid layer. *J. Fluid Mech.* 542, 1–23.
- Howland, C.J., Antkowiak, A., Castrejon-Pita, J.R., Howison, S.D., Oliver, J.M., Style, R.W., Castrejon-Pita, A.A., 2016. It's harder to splash on soft solids. *Phys. Rev. Lett.* 117, 184502.
- Khabakhpasheva, T.I., Korobkin, A.A., 2020. Splashing of liquid droplet on a vibrating substrate. *Phys. Fluids* 32 (12), 122109.
- Kim, J.-H., Rothstein, J.P., 2016. Droplet impact dynamics on lubricant-infused superhydrophobic surfaces: The role of viscosity ratio. *Langmuir* 32 (40), 10166–10176.
- Kim, P., Wong, T.-S., Alvarenga, J., Kreder, M.J., Adorno-Martinez, W.E., Aizenberg, J., 2012. Liquid-infused nanostructured surfaces with extreme anti-ice and anti-frost performance. *ACS Nano* 6 (8), 6569–6577.
- Laney, S.K., Michalska, M., Li, T., Ramirez, F.V., Portnoi, M., Oh, J., Thayne, I.G., Parkin, I.P., Tiwari, M.K., Papakonstantinou, I., 2021. Delayed lubricant depletion of slippery liquid infused porous surfaces using precision nanostructures. *Langmuir* 37 (33), 10071–10078.
- Latka, A., Strandburg-Peshkin, A., Driscoll, M.M., Stevens, C.S., Nagel, S.R., 2012. Creation of prompt and thin-sheet splashing by varying surface roughness or increasing air pressure. *Phys. Rev. Lett.* 109, 054501.
- Lee, C., Kim, H., Nam, Y., 2014. Drop impact dynamics on oil-infused nanostructured surfaces. *Langmuir* 30 (28), 8400–8407.
- Li, J., Ueda, E., Paulssen, D., Levkin, P.A., 2019. Slippery lubricant-infused surfaces: Properties and emerging applications. *Adv. Funct. Mater.* 29 (4), 1802317.
- Maitra, T., Antonini, C., Tiwari, M.K., Mularczyk, A., Imeri, Z., Schoch, P., Poulikakos, D., 2014a. Supercooled water drops impacting superhydrophobic textures. *Langmuir* 30 (36), 10855–10861.
- Maitra, T., Tiwari, M.K., Antonini, C., Schöck, F.V., Jung, S., Eberle, P., Poulikakos, D., 2014b. On the nanoengineering of superhydrophobic and impalement resistant surface textures below the freezing temperature. *Nano Lett.* 14 (1), 172–182.
- Moreira, A., Moita, A., Panão, M., 2010. Advances and challenges in explaining fuel spray impingement: How much of single droplet impact research is useful? *Prog. Energy Combust. Sci.* 36 (5), 554–580.
- Mousavi, S., Pitchumani, R., 2022. A comparative study of mechanical and chemical durability of non-wetting superhydrophobic and lubricant-infused surfaces. *Colloids Surf. A* 643, 128711.

- Muschi, M., Brudieu, B., Teisseire, J., Sauret, A., 2018. Drop impact dynamics on slippery liquid-infused porous surfaces: influence of oil thickness. *Soft Matter* 14, 1100–1107.
- Negus, M.J., Moore, M.R., Oliver, J.M., Cimpeanu, R., 2021. Droplet impact onto a spring-supported plate: analysis and simulations. *J. Eng. Math.* 128 (3).
- Pasandideh-Fard, M., Qiao, Y.M., Chandra, S., Mostaghimi, J., 1996. Capillary effects during droplet impact on a solid surface. *Phys. Fluids* 8 (3), 650–659.
- Pegg, M., Purvis, R., Korobkin, A., 2018. Droplet impact onto an elastic plate: a new mechanism for splashing. *J. Fluid Mech.* 839, 561–593.
- Peppou-Chapman, S., Hong, J.K., Waterhouse, A., Neto, C., 2020. Life and death of liquid-infused surfaces: a review on the choice, analysis and fate of the infused liquid layer. *Chem. Soc. Rev.* 49, 3688–3715.
- Philippi, J., Lagrée, P.-Y., Antkowiak, A., 2016. Drop impact on a solid surface: short-time self-similarity. *J. Fluid Mech.* 795, 96–135.
- Preston, D.J., Song, Y., Lu, Z., Antao, D.S., Wang, E.N., 2017. Design of lubricant infused surfaces. *ACS Appl. Mater. Interfaces* 9 (48), 42383–42392.
- Quéré, D., 2005. Non-sticking drops. *Rep. Prog. Phys.* 68 (11), 2495–2532.
- Riboux, G., Gordillo, J.M., 2014. Experiments of drops impacting a smooth solid surface: A model of the critical impact speed for drop splashing. *Phys. Rev. Lett.* 113, 024507.
- Scolan, Y.-M., Korobkin, A.A., 2001. Three-dimensional theory of water impact. Part 1. Inverse Wagner problem. *J. Fluid Mech.* 440, 293–326.
- Sett, S., Yan, X., Barac, G., Bolton, L.W., Miljkovic, N., 2017. Lubricant-infused surfaces for low-surface-tension fluids: Promise versus reality. *ACS Appl. Mater. Interfaces* 9 (41), 36400–36408.
- Smith, J.D., Dhiman, R., Anand, S., Reza-Garduno, E., Cohen, R.E., McKinley, G.H., Varanasi, K.K., 2013. Droplet mobility on lubricant-impregnated surfaces. *Soft Matter* 9, 1772–1780.
- Stoddard, R., Nithyanandam, K., Pitchumani, R., 2022. Fabrication and durability characterization of superhydrophobic and lubricant-infused surfaces. *J. Colloid Interface Sci.* 608, 662–672.
- Taylor, G.I., 1959. The dynamics of thin sheets of fluid. III. Disintegration of fluid sheets. *Proc. R. Soc. Lond. Ser. A Math. Phys. Eng. Sci.* 253, 313–321.
- Wagner, H., 1932. Über Stoß- und Gleitvorgänge an der Oberfläche von Flüssigkeiten. *Z. Angew. Math. Mech. (ZAMM)* 12 (4), 193–215.
- Wang, L., Gong, Q., Zhan, S., Jiang, L., Zheng, Y., 2016. Robust anti-icing performance of a flexible superhydrophobic surface. *Adv. Mater.* 28, 7729–7735.
- Wang, L., Zhang, R., Zhang, X., Hao, P., 2017. Numerical simulation of droplet impact on textured surfaces in a hybrid state. *Microfluid. Nanofluid.* 21, 61.
- Wang, L.-Z., Zhou, A., Zhou, J.-Z., Chen, L., Yu, Y.-S., 2021. Droplet impact on pillar-arrayed non-wetting surfaces. *Soft Matter* 17, 5932–5940.
- Wong, T.-S., Kang, S.H., Tang, S.K.Y., Smythe, E.J., Hatton, B.D., Grinthal, A., Aizenberg, J., 2011. Bioinspired self-repairing slippery surfaces with pressure-stable omniphobicity. *Nature* 477, 443–447.
- Wu, Z., Cao, Y., 2017. Dynamics of initial drop splashing on a dry smooth surface. *PLoS One* 12, 1–11.
- Xu, L., Barcos, L., Nagel, S.R., 2007. Splashing of liquids: Interplay of surface roughness with surrounding gas. *Phys. Rev. E* 76, 066311.
- Yeganehdoust, F., Attarzadeh, R., Dolatabadi, A., Karimfazli, I., 2021. A comparison of bioinspired slippery and superhydrophobic surfaces: Micro-droplet impact. *Phys. Fluids* 33 (2), 022105.
- Zeng, X., Guo, Z., Liu, W., 2021. Recent advances in slippery liquid-infused surfaces with unique properties inspired by nature. *Bio-Des. Manuf.* 4, 506–525.
- Zhang, P., Lin, L., Zang, D., Guo, X., Liu, M., 2017. Designing bioinspired anti-biofouling surfaces based on a superwettability strategy. *Small* 13 (4), 1503334.
- Zhang, M., Sun, G., Guo, H., Liu, Q., Liu, J., Yu, J., Chen, R., Gao, L., Wang, J., 2020. Effect of morphology evolution on the anticorrosion performance of superhydrophobic surfaces and lubricant-infused surfaces. *ACS Sustain. Chem. Eng.* 8 (8), 3170–3180.